Partial-wave analysis of nucleon-nucleon elastic scattering data

Ron L. Workman, William J. Briscoe, and Igor I. Strakovsky

Phys. Rev. C **94**, 065203 — Published 19 December 2016

DOI: 10.1103/PhysRevC.94.065203

Partial-Wave Analysis of Nucleon-Nucleon Elastic Scattering Data

Ron L. Workman,[1] William J. Briscoe,[1] and Igor I. Strakovsky[1]

[1] *Institute for Nuclear Studies, Department of Physics, The George Washington University, Washington, D.C. 20052*

(Dated: November 22, 2016)

Energy-dependent and single-energy fits to the existing nucleon-nucleon database have been updated to incorporate recent measurements. The fits cover a region from threshold to 3 GeV, in the laboratory kinetic energy, for proton-proton scattering, with an upper limit of 1.3 GeV for neutron-proton scattering. Experiments carried out at the COSY-WASA and COSY-ANKE facilities have had a significant impact on the partial-wave solutions. Results are discussed in terms of both partial-wave and direct reconstruction amplitudes.

PACS numbers: 11.80.Et, 13.75.Cs, 25.40.Cm, 25.40.Dn

I. INTRODUCTION

The nucleon-nucleon interaction is fundamental to the understanding of nuclear physics as a whole. The elastic scattering of protons and neutrons, at low to medium energies, can be analyzed in terms of a partial-wave expansion, yielding amplitudes that are valuable for comparison to models [1] and also as input to more complex processes, such as proton-deuteron scattering [2] and deuteron electro-disintegration [3]. Fit results have also been used in Monte Carlo simulations and incorporated into geometry and tracking of the Geant4 simulation [4] software, a basic tool for low, medium, and high energy groups.

In nucleon-nucleon elastic scattering, as the initial and final state particles all have spin 1/2, many independent observables are available [5] and have been measured over decades of systematic studies at ANL, COSY, IUCF, LAMPF, PSI, SATURN, TRIUMF, TUNL and other facilities. This has allowed a direct scattering amplitude reconstruction (DAR) [6, 7] at a number of energies and angles. We compare our results with these reconstructions below.

Our last published analysis [8] (SP07) of the nucleon-nucleon database was completed in 2007 and largely motivated by data provided by the EDDA Collaboration [9–11], with some data also coming from the SATURNE II and PNPI groups. The most recent measurements have been fewer in number but greater in effect. This is true for both *pp* and *np* scattering.

Recent COSY-WASA measurements [12, 13] of the *np* scattering observable, A_y, have shown a sharp energy dependence, over a narrow energy range, when combined with the trend displayed by existing lower-energy data [14]. This behavior was not predicted by the SP07 analysis, nor was it seen in previous fits [15–18]. In a revised fit [12], this narrow structure was reproduced with the generation of a pole, at $[(2380 \pm 10) - i(40 \pm 5)]$ MeV in the coupled ${}^3D_3$–${}^3G_3$ partial waves, closely related to the resonance mass and width ($M \approx 2380$ MeV , $\Gamma \approx 70$ MeV), deduced from WASA analyses of related two-pion production measurements [19].

We subsequently compared the predictions of fits to *np* scattering data, with and without a pole, to search for other potentially sensitive observables [13]. Experimental tests are limited by the existing *np* database, which supports a partial wave analysis (PWA) only up to a laboratory kinetic energy of 1.3 GeV. No single measurement is capable of extending the range of PWAs. A programmatic study would be required and this is unlikely to occur in the near future.

For *pp* elastic scattering, measurements of near-forward differential cross sections [20] and the polarization quantity [21], A_y, from the COSY-ANKE Collaboration, were poorly predicted by the SP07 fit. The simple inclusion of these data in the full database did not generally result in a significant improvement. Below we discuss the fitting strategy and its connection to recent (SP07) [8] and older (SM97) [15] PWA results.

II. FITS TO DATA

The SP07 analysis is accessible via the Scattering Analysis Interactive Database (SAID) website [22]. The fit form is based on the product of exchange and production S-matrices. The exchange piece is parametrized via a K-matrix and contains a one-pion exchange term plus a sum over expansion bases containing a left-hand cut. The production piece is parametrized in terms of a Chew-Mandelstam K-matrix and allows for the production of an inelastic channel. For the isovector waves, the inelasticity is assumed to be dominated by the $N\Delta$ channel. For isoscalar waves, there is an effective second channel. The formalism for both spin-coupled and uncoupled waves is explained in detail in Refs. [15, 23].

The χ^2 fit to data is carried out, using the form

$$\chi^2 = \sum_i \left(\frac{N\Theta_i - \Theta_i^{\rm exp}}{\epsilon_i} \right)^2 + \left(\frac{N-1}{\epsilon_N} \right)^2 , \qquad (1)$$

where $\Theta_i^{\rm exp}$ is an experimental point in an angular distribution, with associated statistical error ϵ_i, and Θ_i is the fit value. Here the overall systematic error, ϵ_N, is used to weight an additional χ^2 penalty term due to the

renormalization of angular distributions in the fit by the factor N.

The partial-wave solution (SP07) was determined through a fit to approximately 25 thousand pp data (to 3 GeV) and 13 thousand np data (to 1.3 GeV). Compared to the recent np [12] and pp [21] A_y measurements, SP07 predicted a different forward-angle behavior, for pp data, and a different shape at the energy corresponding to the proposed WASA dibaryon, for np data. SP07 was able to reproduce the angular behavior of the new and very precise forward pp cross sections [20], but the resulting renormalization factors (N), for several energies, were outside the range expected from the quoted overall systematic errors.

Different strategies were used to accommodate the new np and pp scattering data. For the pp A_y observable, an improved fit was achieved by more heavily weighting the new data, by a factor of 4, in the fit. Conversely, for the cross sections, the second term in Eq. 1 was increased in weight until the fitted renormalization factors deviated from unity by an amount consistent with the quoted systematic errors. Weighting was also used to study the influence of the COSY-WASA np A_y data, as has been described in Refs. [12, 13].

In Fig. 1, we plot the fits SP07, an unweighted fit (SM16), and a weighted fit (WF16) to the new forward cross section data [20]. The fit quality for larger-angle COSY measurements [9], which were included in the SP07 fit, is displayed as well. In the comparison, the fitted normalization factor has not been applied in order to show how large a factor is required in an unweighted fit, or the SP07 prediction, at the highest energies.

In Fig. 2, the above three partial-wave solutions are compared to the new pp A_y data [21] and other data sets covering the full angular range. In contrast to Fig. 1, the data sets have all been modified according to the renormalization factors found in the weighted fit WF16. Here we see that the new A_y measurements cover an angular range not previously measured, are much more precise than earlier measurements and, in some cases, differ from those earlier measurements at angles where there is overlap.

In the revised solutions SM16 and WF16, the fit quality for total cross sections was also addressed. In Fig. 3, we plot the total cross section ($\sigma^{\rm tot}$), the total reaction cross section ($\sigma_{\rm R}^{\rm tot}$), the difference between total cross sections in pure transverse-spin states

$$\Delta\sigma_T^{\rm tot} = \sigma^{tot}(\uparrow\downarrow) - \sigma^{tot}(\uparrow\uparrow), \qquad (2)$$

and the difference between total cross sections in pure longitudinal-spin states

$$\Delta\sigma_L^{\rm tot} = \sigma^{tot}(\leftarrow\rightarrow) - \sigma^{tot}(\rightarrow\rightarrow). \qquad (3)$$

Several comments are in order. The total reaction cross section [25, 26] is not a pure measurement and has not been included in these fits. It is, however, qualitatively

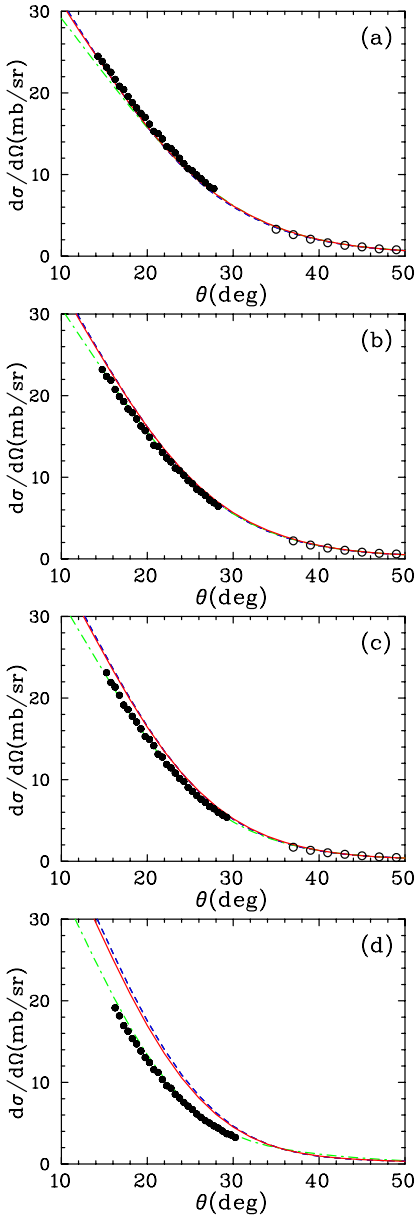

FIG. 1: (Color online) Cross sections for pp elastic scattering. Data from the SAID database [22]. Recent COSY data plotted as solid black circles: (a) 2000 MeV, (b) 2200 MeV, (c) 2400 MeV, and (d) 2800 MeV; older COSY data within ±4 MeV shown as open black circles. Red solid (green long dot-dashed) lines, correspond to the recent SM16 (WF16) solution. The previous SP07 [8] solution is plotted with blue dashed lines.

well predicted. The quantity $\Delta\sigma_T^{\rm tot}$ is not well reproduced by the SP07 solution and was given added weight in the SM16 and WF16 fits. In contrast, $\Delta\sigma_L^{\rm tot}$ is reasonably well represented by all the displayed fits. The total cross section $\sigma^{\rm tot}$ dataset includes some extremely precise measurements [24] (with statistical errors of the order of 0.1%) which can dominate the χ^2 in a fit. In the SP07 fit, subsets of energies in the measurement of Ref. [24]

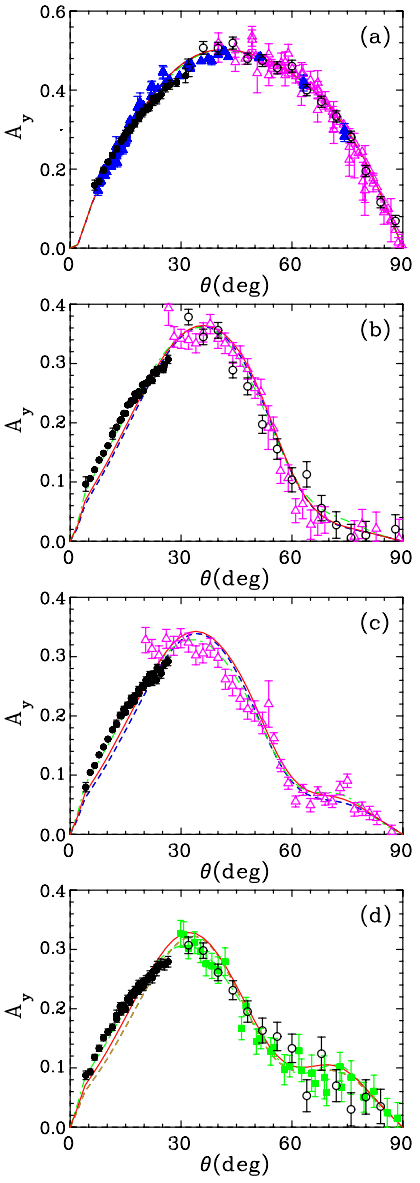

FIG. 2: (Color online) Polarized observable A_y for pp elastic scattering. Recent COSY data plotted as solid black circles: (a) 796 MeV, (b) 1600 MeV, (c) 1800 MeV, and (d) 1965 MeV. Data within ±8 MeV from the SAID database [22] (COSY, SATURN, LAMPF, and ANL) shown as open black circles, open magenta triangles, solid blue triangles, and solid green squares. Notation for energy dependent fits as in Fig. 1.

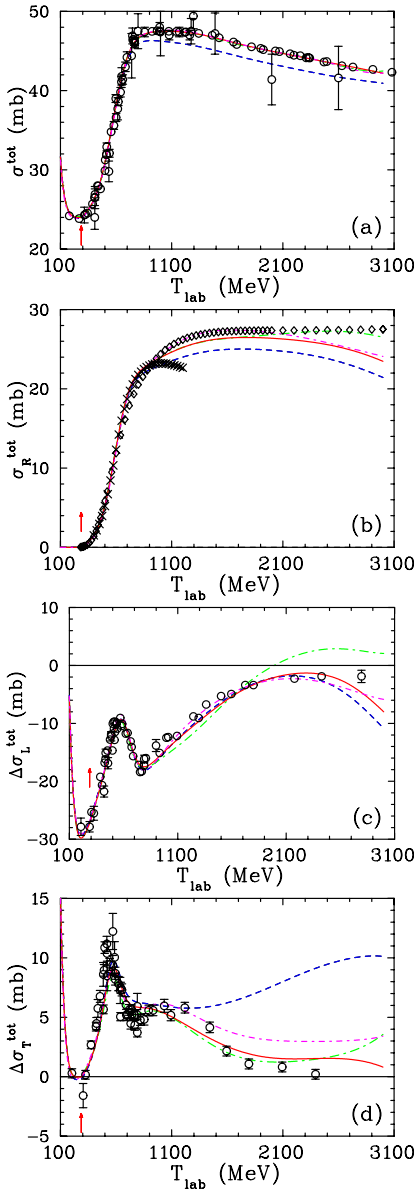

FIG. 3: (Color online) Total unpolarized (a) and (b) and polarized (c) and (d) cross sections for pp scattering. Quasi-data for total reaction cross sections from Refs. [25] and [26] are given by black crosses and open diamonds, respectively. Pion production threshold shown as a vertical red arrow. Notation for energy dependent fits as in Fig. 1. Additionally, the older SM97 solution [15] is plotted as magenta short dot-dashed lines.

were allowed to have a common renormalization, resulting in a curve systematically below these data. In the present fit, this renormalization freedom was removed. As a result, the fits SM16 and WF16 are nearly identical for this quantity. For comparison purposes, the older fit SM97 [15] has been plotted as well. Below we will see that the quality of fit to total cross section quantities is reflected in a variability for the $^1S_0$ partial wave amplitude.

In addition to global fits to all data from threshold to 3 GeV and 1.3 GeV, in $T_{\rm lab}$, for pp and np scattering data, respectively, a set of single-energy solutions (SES) was also generated. Here, data within narrow energy bins are searched, starting from the global fit, without the constraint of energy-to-energy smoothness. This allows a search for systematic deviations from the global fit. As a point of comparison, we display the number of data in a histogram, for both pp and np scattering, in Fig. 4, together with the number of measured observ-

ables. Clearly, the data constraints for a global fit are significantly reduced beyond 1.1 GeV, for *np* scattering, and beyond about 2.5 GeV, for *pp* scattering. In Fig. 5, the χ^2 difference between global and single-energy fits is also compared. This gives a qualitative picture of the fit stability which, as expected, improves with the number of data constraints. -

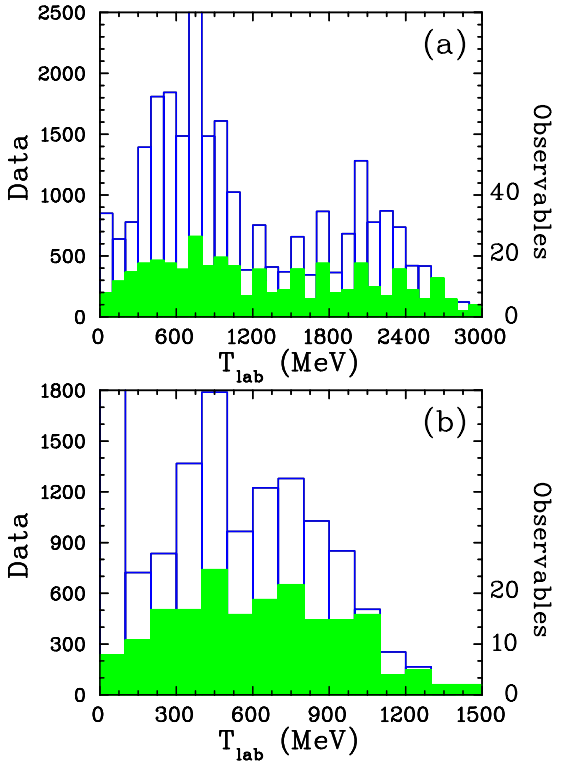

FIG. 4: (Color online) Histograms (a) for *pp* scattering data (open blue bars) and observable types (filled green bars) and (b) for *np* data in the same notation.

III. AMPLITUDES

We are using the notation of Ref. [6, 7] and write the scattering matrix, $M(\vec{k}_f, \vec{k}_i)$, as

$$\begin{aligned} M(\vec{k}_f, \vec{k}_i) &= \frac{1}{2}[(a+b) + (a-b)\ (\vec{\sigma}_1 \cdot \vec{n})\ (\vec{\sigma}_2 \cdot \vec{n}) \\ &+ (c+d)\ (\vec{\sigma}_1 \cdot \vec{m})\ (\vec{\sigma}_2 \cdot \vec{m}) \\ &+ (c-d)\ (\vec{\sigma}_1 \cdot \vec{l})\ (\vec{\sigma}_2 \cdot \vec{l}) \\ &+ e\ (\vec{\sigma}_1 + \vec{\sigma}_2) \cdot \vec{n}], \end{aligned}$$

where $\vec{k}_f$ and $\vec{k}_i$ are the scattered and incident momenta in the c.m. system, and

$$\vec{n} = \frac{\vec{k}_i \times \vec{k}_f}{|\vec{k}_i \times \vec{k}_f|}\ ,\ \vec{l} = \frac{\vec{k}_i + \vec{k}_f}{|\vec{k}_i + \vec{k}_f|}\ ,\ \vec{m} = \frac{\vec{k}_f - \vec{k}_i}{|\vec{k}_f - \vec{k}_i|}.$$

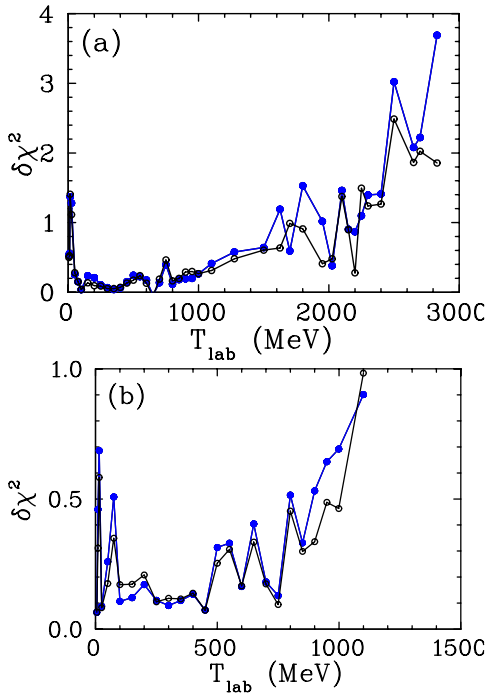

FIG. 5: (Color online) Comparison of the SES and energy dependent (ED) fits in terms of $\delta\chi^2 = [\chi^2(ED) - \chi^2(SES)]$/data for (a) *pp* and (b) *np* data. The SM16 and SP07 ED fits are displayed as blue solid and black open symbols, respectively.

Writing the scattering matrix in this form, any *pp* observable can be expressed in terms of the five complex amplitudes a through e. If a sufficient number of independent observables are measured precisely at a given energy and angle, these amplitudes can be determined up to an overall undetermined phase. The advantage of this method is its model independence; nothing beyond the data is required to determine a solution. In addition, once the amplitudes are found, any further experimental quantity can be predicted at the energy-angle points of the DAR. In practice, however, experimental uncertainties allow for multiple solutions comparable in their representation of the data.

In Figs. 6 through 9, the *pp* DAR amplitudes a through e of Ref. [6] are plotted for energies between 1.8 and 2.7 GeV. These amplitudes have an overall phase ambiguity which is resolved, in the plots, by taking the e amplitude to be real. At the highest energy, with fewer data and observable types available, results are only plotted at a pair of angles. At the other energies, however, where multiple solutions form separate branches, the fits SM16 and WF16 tend to branch as well. The DAR amplitudes of Ref. [7] for *np* scattering, from 0.8 to 1.1 GeV, show good overall agreement with the plotted fits. These are displayed in Figs. 10–15.

In Figs. 16 and 17, the dominant isovector PWA results are plotted. Here we compare the previous SP07

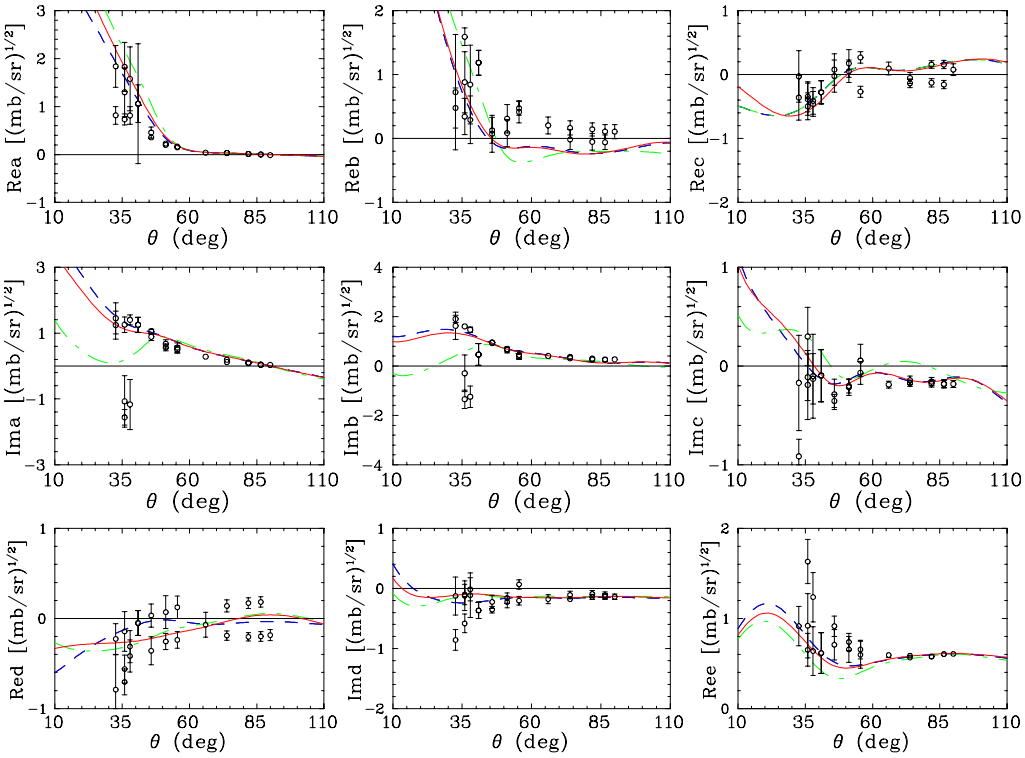

FIG. 6: (Color online) DAR of a to e for pp elastic scattering at $T_{lab} = 1.8$ GeV as a function of c.m. scattering angle. Real and imaginary parts of the Saclay amplitudes [6] are shown as black open circles. Notation for SAID energy-dependent amplitudes as in Fig. 1.

result to the present SM16 and WF16 fits. Unlike the DAR results, a PWA is not strictly model-independent and variations between fits are expected with the onset of inelasticity and an increasing angular momentum cutoff. However, for values of T_{Lab} below 1 GeV, fits have remained very stable. The largest deviations are generally found in smaller partial waves and at the highest fitted energies. Results for these and previous fits may be found on the SAID website, together with the associated database [22].

In Fig. 16, the dimensionless T-matrices are plotted for the global fits and the SES results. The fits SM16 and SP07 are qualitatively similar and fall within the scatter of the SES values. The weighted fit, WF16, constrained to better reproduce the recent measurements, shows significant deviations from SM16 in the $^1S_0$ and $^1D_2$ partial waves. This effect was noted in Ref. [20]. The behavior of the $^1S_0$ wave is remarkably similar to the much older fit, SM97, completed in 1997. As displayed in Fig. 3, SM97 followed the polarized and unpolarized total cross sections more closely than SP07. Thus, we find the $^1S_0$ wave to be particularly sensitive to constraints imposed to fit the total cross sections and the forward differential cross sections.

In Fig. 17, selected phase shifts are plotted for both the global and SES fits and are compared to results from the Saclay SES [6]. All determinations agree quite well below 500 MeV and begin to scatter significantly above 1 GeV. A significant deviation between the SM16 and WF16 fits is visible in the $^3F_2$ and this was noted, in Ref. [21], to be the result of constraints imposed by the recent forward A_y measurements [21].

The dominant isoscalar partial-wave amplitudes are plotted in Figs. 18 and 19. As for the isovector waves, we first plot the global fits and SES in terms of the dimensionless T-matrices. Here, for the coupled $^3D_3$–$^3G_3$ partial waves, we also plot the fit containing an associated pole for comparison. This feature has been extensively discussed in Refs. [12, 13]. Phase shifts are plotted for selected waves in Fig. 19. As was the case for the isovector amplitudes, all determinations, including the Saclay PWA [7] agree well up to 500 MeV.

IV. SUMMARY AND CONCLUSIONS

We have fitted recent precise measurements of the pp differential cross sections and the observable A_y, both at forward angles, together with np A_y data near the limit of our isoscalar PWA. The energy dependence implied by the new np data, together with older measurements,

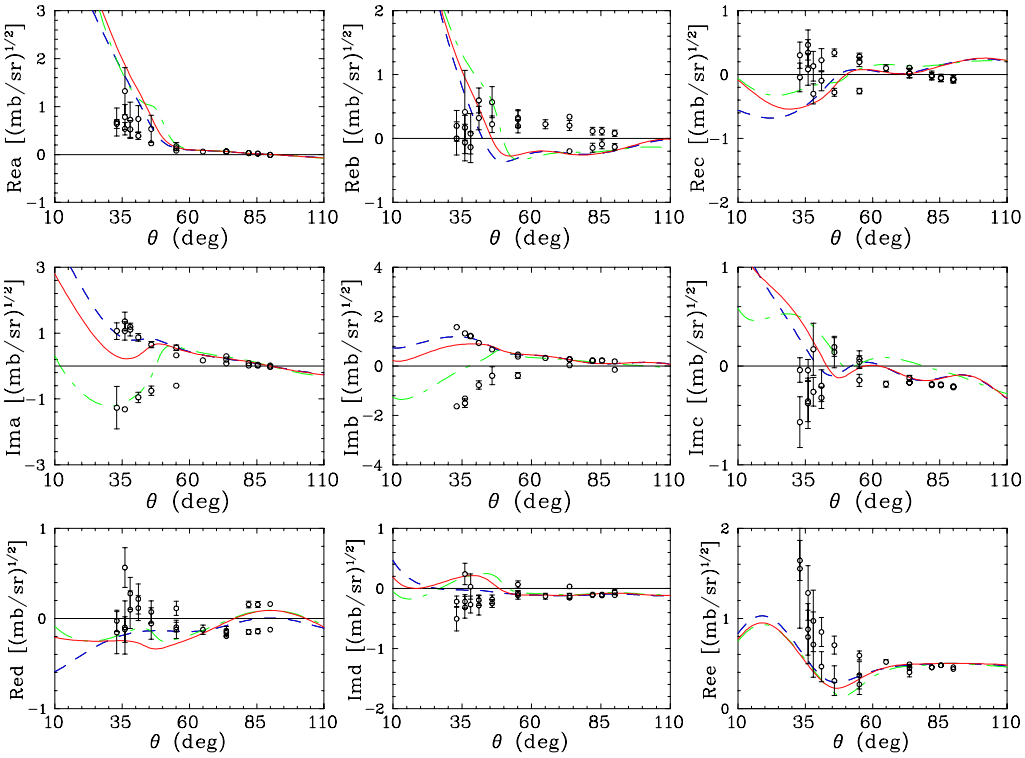

FIG. 7: (Color online) DAR of a to e for pp elastic scattering at $T_{lab} = 2.1$ GeV as a function of c.m. scattering angle. Notation as in Fig. 6.

suggest a rapid variation that has been accommodated through the generation of a pole, providing supporting evidence for the WASA dibaryon candidate. Little additional np data has been added to the SAID database since the 2007 PWA and the sharp structure in A_y is localized to a narrow energy range. As a result, the amplitudes - apart from the coupled ${}^3D_3$–${}^3G_3$ partial waves - have changed little since the last published analysis. At the level of a DAR, we are consistent with the Saclay analysis. However, the upper limit for our np PWA (1.3 GeV) is much below the pp PWA upper limit (3.0 GeV).

The pp DAR comparison has been made at a higher set of energies and here multiple solutions appear to form branches that are chosen differently by the present SM16 and WF16 fits. The SM16 and WF16 fits also differ at the PWA level, particularly in the ${}^1S_0$, ${}^1D_2$, and ${}^3F_2$ amplitudes. The largest difference, in the ${}^1S_0$ wave, is very sensitive to the fit quality associated with the polarized and unpolarized pp total cross sections, together with the fit to near-forward pp differential cross sections. The present SM16 and WF16 solutions differ significantly from SP07 in their fit to these observables. We have also observed that the fit WF16 has a ${}^1S_0$ partial wave remarkably similar to that found in the older SM97 solution, which featured a different treatment of the total cross sections.

The weighted fit, WF16, was constructed to improve the description of new cross section and A_y data. However, by increasing the weight of new data, older data are implicitly given less weight, resulting in a degraded fit. This produces a higher overall χ^2/datum for the full database. For values of $T_{\rm lab}$ from threshold to 350 MeV, the potential model region, all fits are virtually identical, giving a χ^2/datum of about 1.25 for pp over the full database. For pp scattering up to 1 GeV, the χ^2/datum increases to about 1.5, compared to a value slightly below 2.0 for the SM16 fit covering the full pp scattering range from threshold to 3 GeV.

We note that the Nijmegen partial-wave and potential model analyses [27] of pp scattering data achieved a χ^2/datum closer to unity over a more restricted dataset and energy range. The Nijmegen low-energy partial waves differ very little from those presented here. Comparisons of the various analyses, including the Nijmegen fit, may be obtained using the SAID website.

Acknowledgments

This work was supported in part by the U.S. Department of Energy, Office of Science, Office of Nuclear Physics, under award numbers DE-SC0014133 and DE-

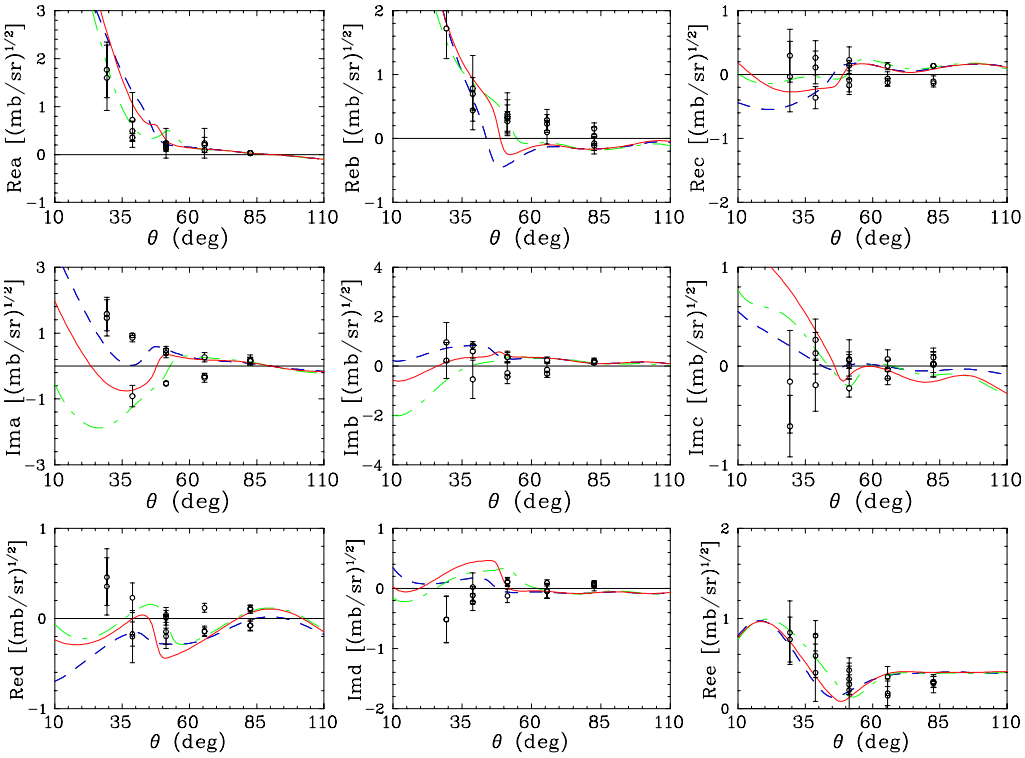

FIG. 8: (Color online) DAR of a to e for pp elastic scattering at $T_{lab} = 2.4$ GeV as a function of c.m. scattering angle. Notation as in Fig. 6.

SC0016582.

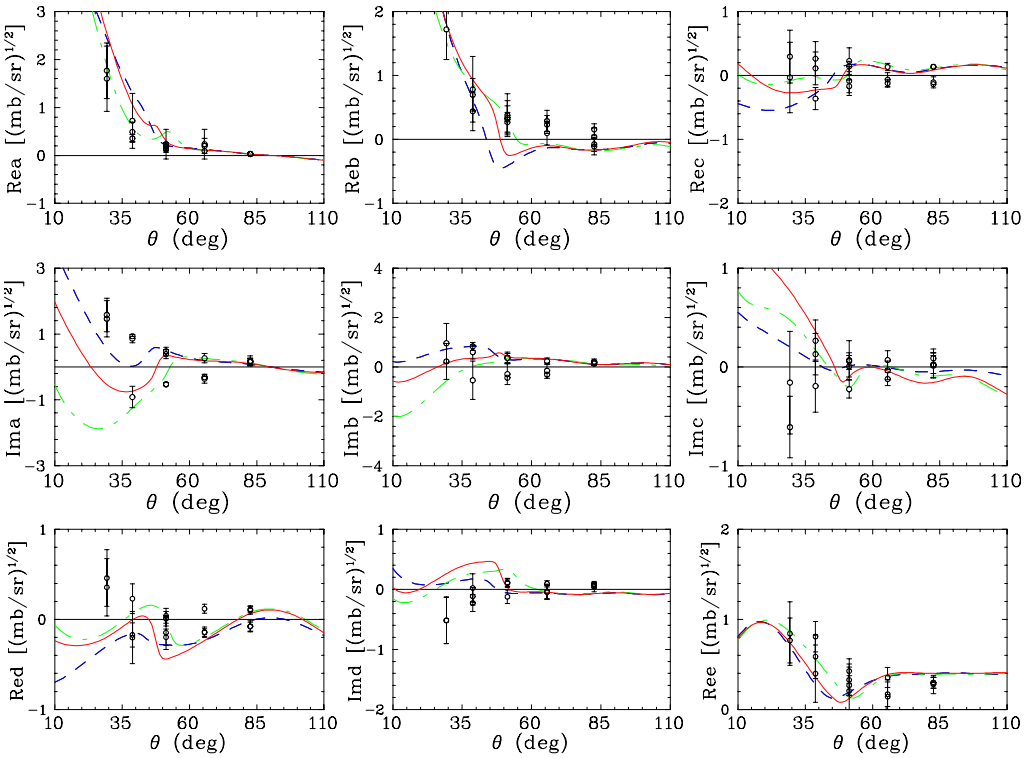

FIG. 9: (Color online) DAR of a to e for pp elastic scattering at $T_{lab} = 2.7$ GeV as a function of c.m. scattering angle. Notation as in Fig. 6.

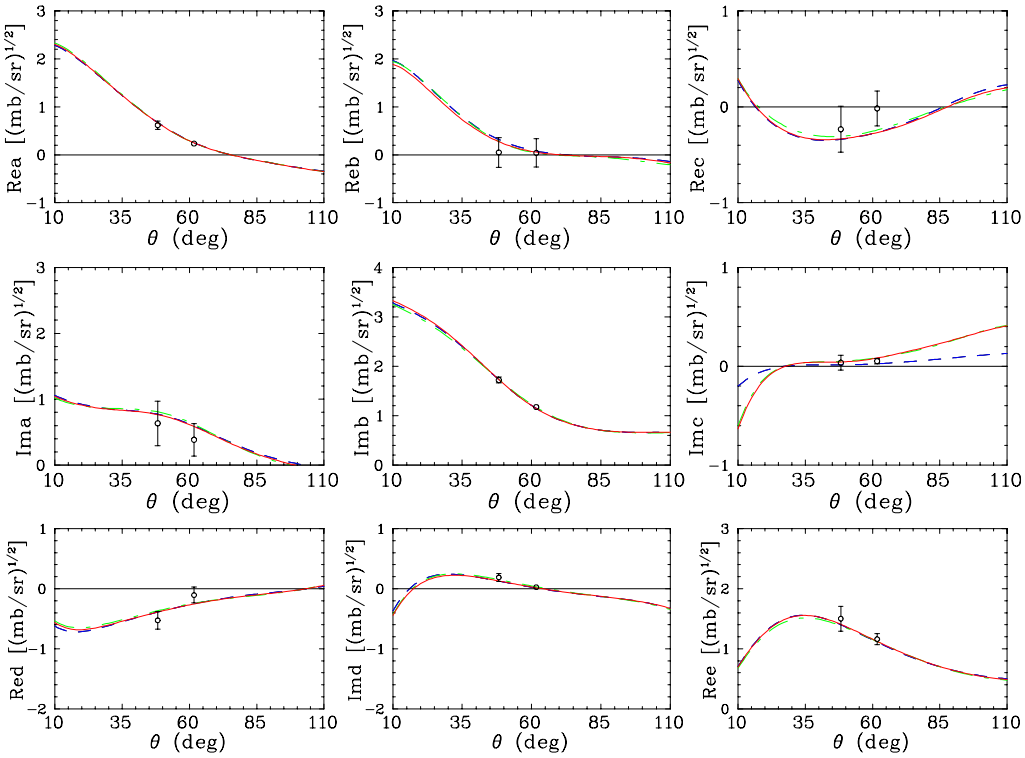

FIG. 10: (Color online) DAR of a to e for np elastic scattering at $T_{lab} = 0.80$ GeV as a function of c.m. scattering angle. Real and imaginary parts of the Saclay amplitudes [7] are shown as black open circles. Notation for SAID amplitudes as in Fig. 1.

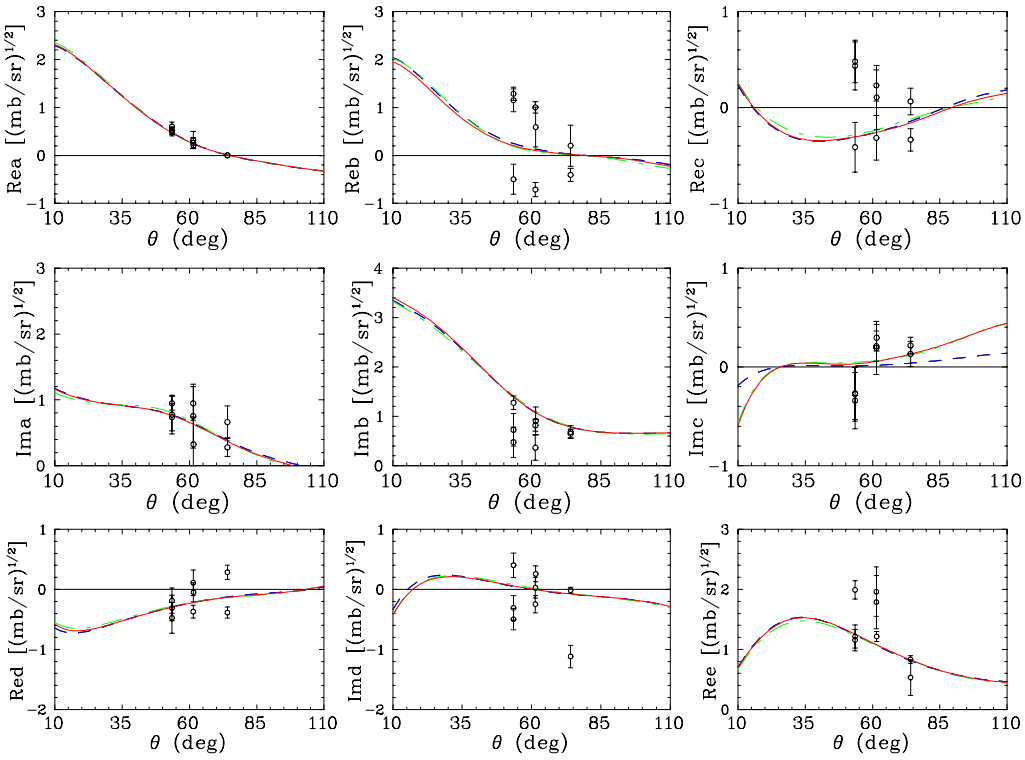

FIG. 11: (Color online) DAR of a to e for np elastic scattering at $T_{lab} = 0.84$ GeV as a function of c.m. scattering angle. Notation as in Fig. 10.

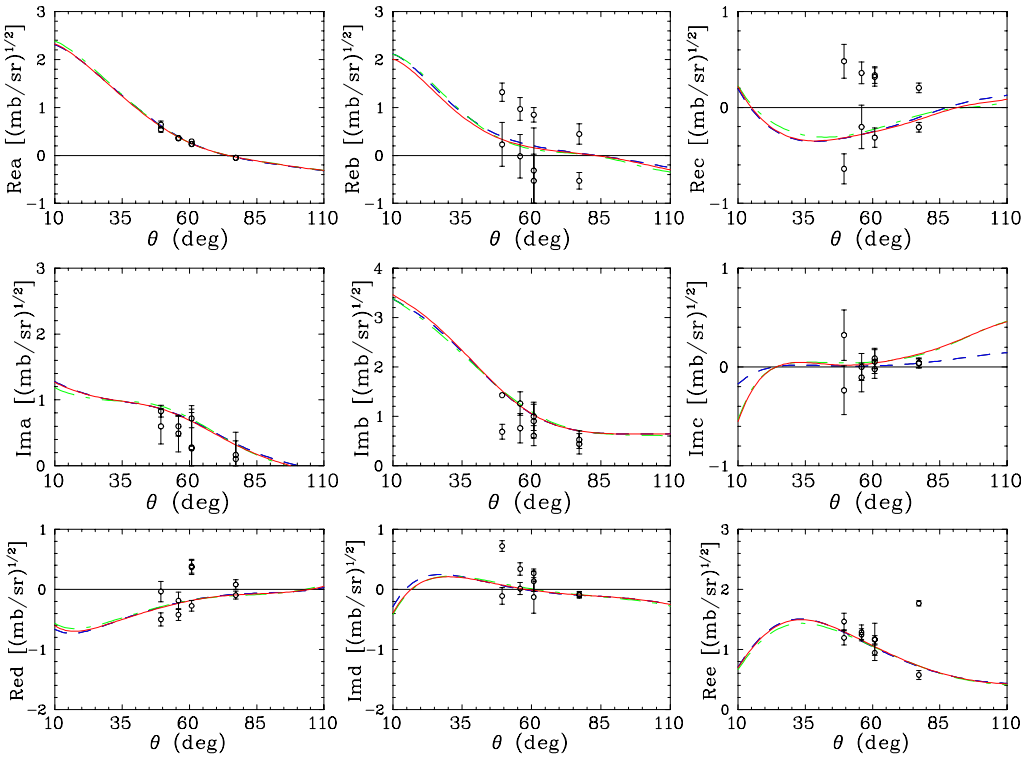

FIG. 12: (Color online) DAR of a to e for np elastic scattering at $T_{lab} = 0.88$ GeV as a function of c.m. scattering angle. Notation as in Fig. 10.

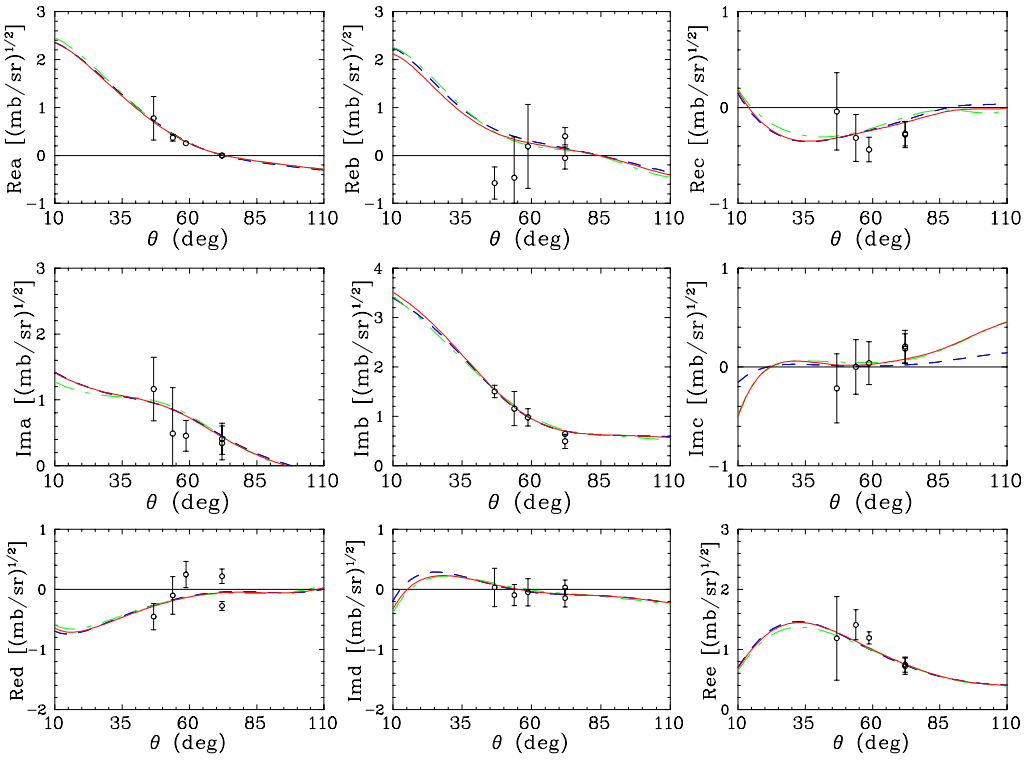

FIG. 13: (Color online) DAR of a to e for np elastic scattering at $T_{lab} = 0.94$ GeV as a function of c.m. scattering angle. Notation as in Fig. 10.

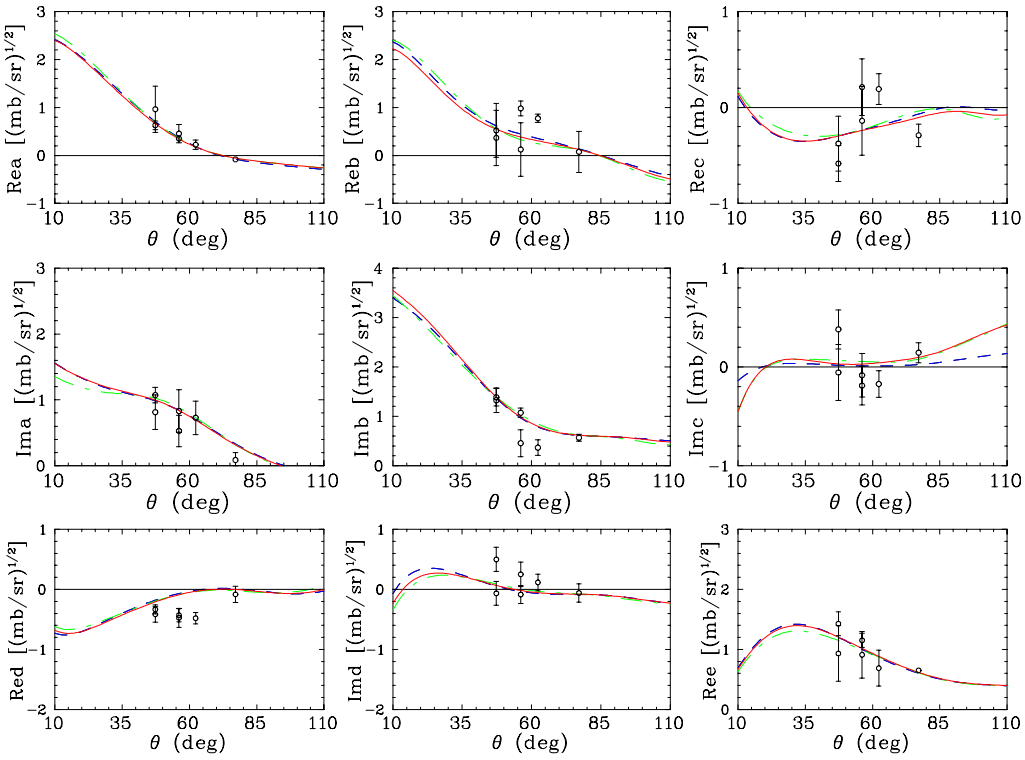

FIG. 14: (Color online) DAR of a to e for np elastic scattering at T_{lab} = 1.00 GeV as a function of c.m. scattering angle. Notation as in Fig. 10.

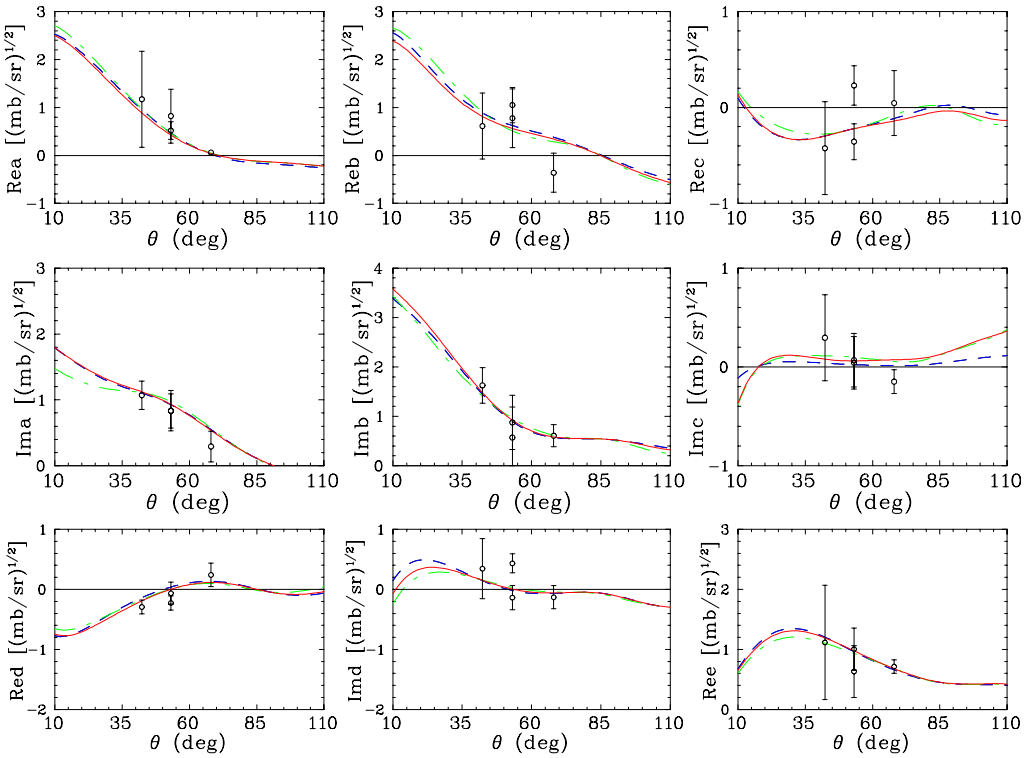

FIG. 15: (Color online) DAR of a to e for np elastic scattering at T_{lab} = 1.10 GeV as a function of c.m. scattering angle. Notation as in Fig. 10.

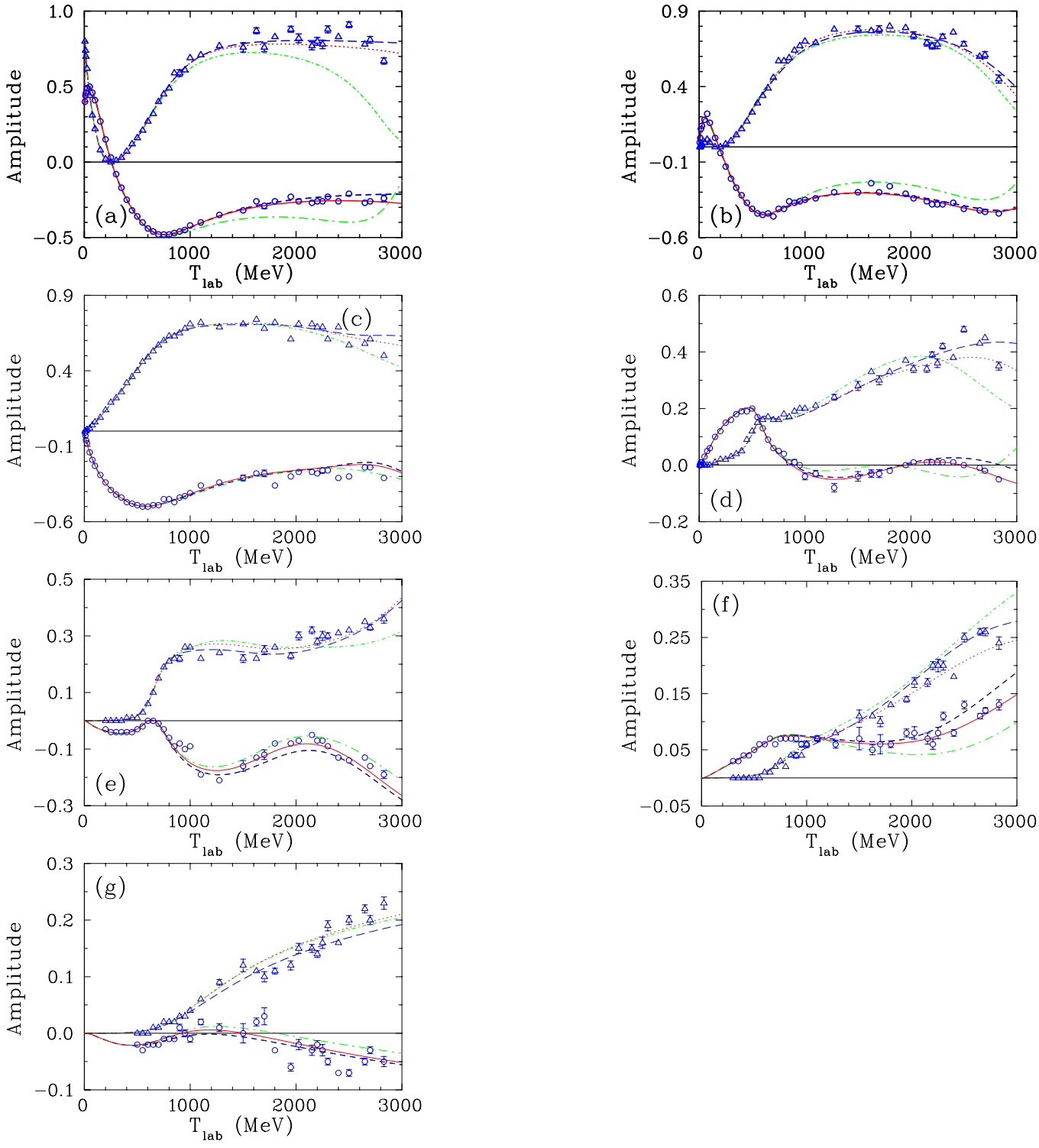

FIG. 16: (Color online) Dominant isovector partial-wave amplitudes from threshold to $T_{lab} = 3$ GeV. (a) $^1S_0$, (b) $^3P_0$, (c) $^3P_1$, (d) $^1D_2$, (e) $^3F_3$, (f) $^1G_4$, and (g) $^3H_5$. Real (imaginary) parts of energy dependent solutions SM16, WF16, and SP07 are plotted as red solid (dotted), green long dot-dashed (short dot-dashed), and blue short-dashed (long-dashed) lines, respectively. Real (imaginary) parts of SES, corresponding to energy dependent fit SM16, are plotted with blue open circles (triangles). All amplitudes are dimensionless.

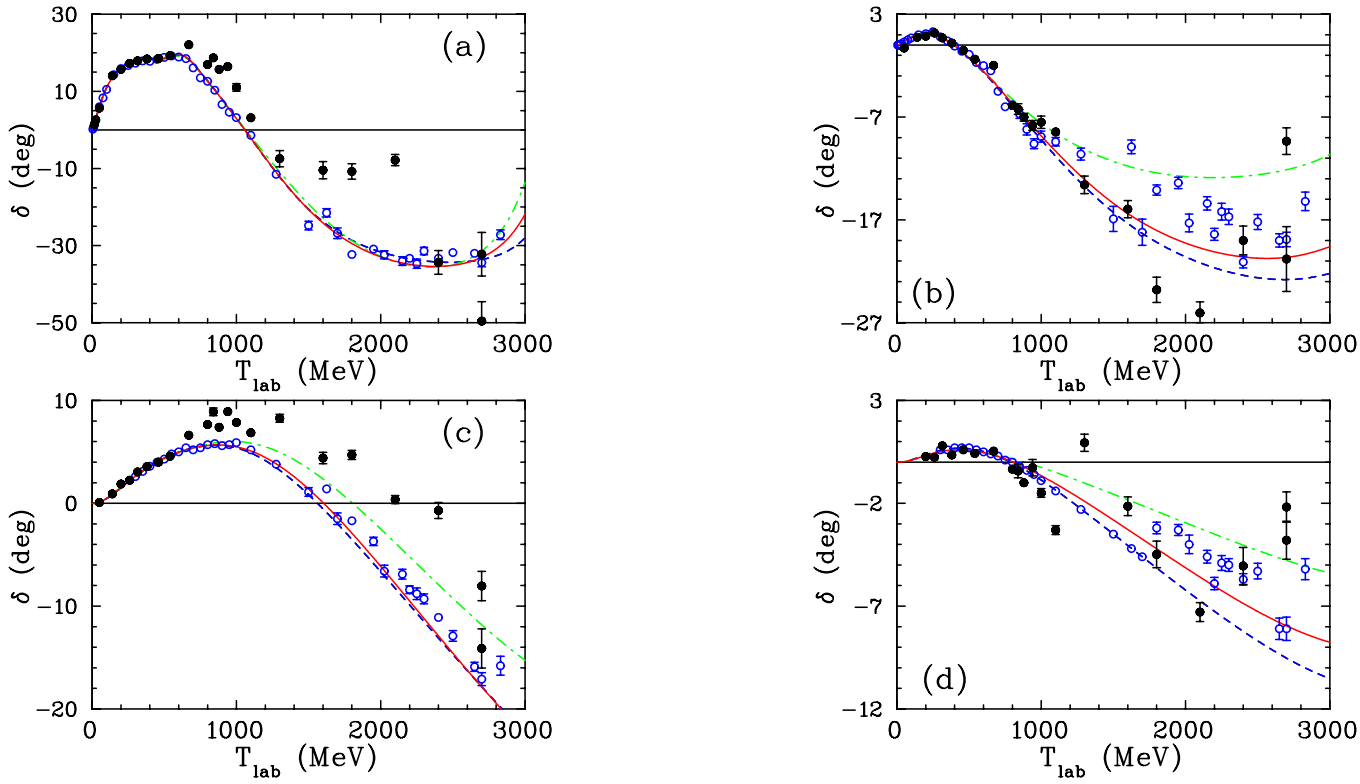

FIG. 17: (Color online) Phase-shift parameters for dominant isovector partial-wave amplitudes from threshold to $T_{lab} = 3$ GeV. (a) $^3P_2$, (b) $^3F_2$, (c) $^3F_4$, and (a) $^3H_4$. Saclay SES phase-shifts [6] are shown as black filled circles; SAID SES are plotted as open blue circles. Notation for SAID energy-dependent amplitudes as in Fig. 1.

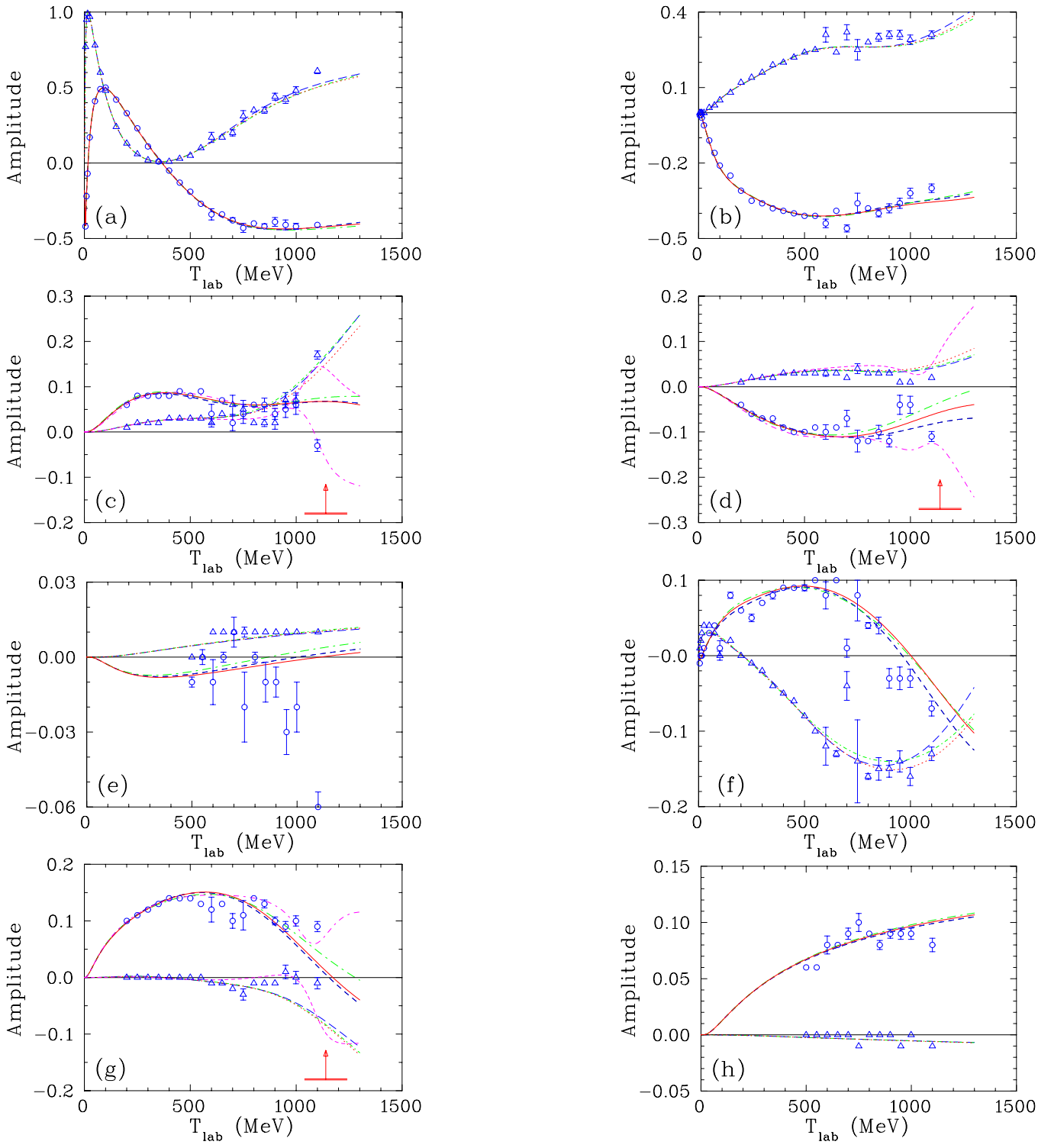

FIG. 18: (Color online) Dominant isoscalar partial-wave amplitudes from threshold to $T_{lab} = 1.3$ GeV. (a) $^3S_1$, (b) $^3D_1$, (c) $^3D_3$, (d) $^3G_3$, (e) $^3G_5$, (f) ϵ_1, (g) ϵ_3, and (h) ϵ_5. Notation as in Fig. 16. Revised SAID solution for $^3D_3$, $^3G_3$, and ϵ_3, with a pole, is plotted as magenta short dot-dashed (short dashed) lines for the real (imaginary) parts. Red vertical arrows indicate the WASA resonance mass W_R value and the red horizontal bar gives the full width Γ [12].

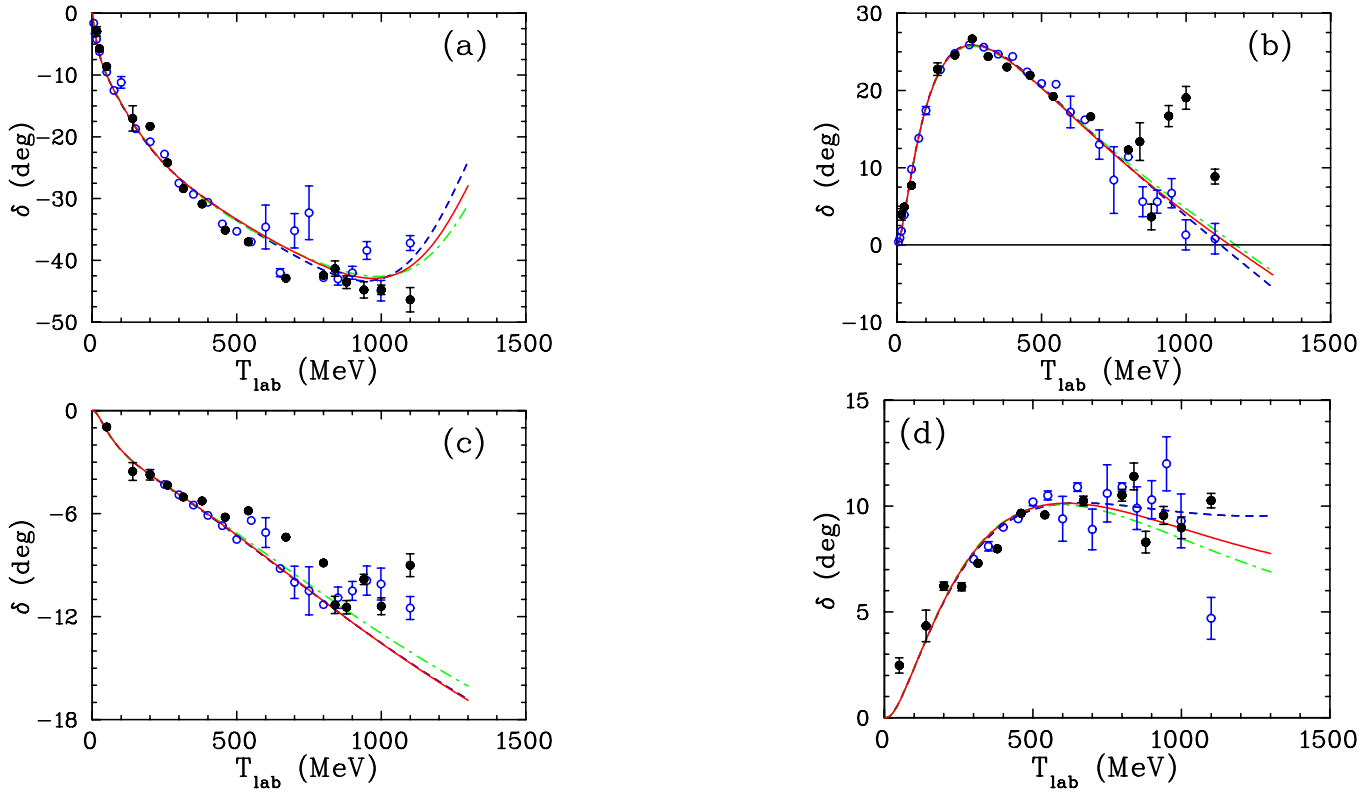

FIG. 19: (Color online) Phase-shift parameters for dominant isoscalar partial-wave amplitudes from threshold to $T_{lab} = 1.3$ GeV. (a) $^1P_1$, (b) $^3D_2$, (c) $^1F_3$, and (d) $^3G_4$. The Saclay SES [7] are given by black filled circles; SAID SES are plotted as open blue circles. Notation for SAID energy-dependent amplitudes as in Fig. 1.

[1] A. M. Shirokov *et al.*, Phys. Rev. C **90**, 024324 (2014); J. J. de Swart, R. A. M. M. Klomp, M. C. M. Rentmeester, and Th. A. Rijken, Few-Body Systems Suppl. **99**, 1 (2008).

[2] S. Dymov *et al.*, Phys. Lett. B **744**, 391 (2015); A. A. Temerbayev and Yu. N. Uzikov, Phys. Atom. Nucl. **78**, 35 (2015).

[3] W. P. Ford, S. Jeschonnek, and J. W. Van Orden, Phys. Rev. C **90**, 064006 (2014); O. Moreno, T. W. Donnelly, J. W. Van Orden, W. P. Ford, Phys. Rev. D **92**, 053006 (2015).

[4] D. H. Wright and M. H. Kelseya (for the Geant4 Hadronic Working Group), Nucl. Instrum. Meth. A **804**, 175 (2016).

[5] J. Bystricky, F. Lehar, and P. Winternitz, J. Phys. (France), **39**, 1 (1978).

[6] J. Bystricky, C. Lechanoine-LeLuc, and F. Lehar, Eur. Phys. J. C **4**, 607 (1998); F. Lehar, private communication, 1998.

[7] J. Ball *et al.*, Il Nuovo Cimento **111A**, 13 (1998); F. Lehar, private communication, 1998.

[8] R. A. Arndt, W. J. Briscoe, I. I. Strakovsky, and R. L. Workman, Phys. Rev. C **76**, 025209 (2007).

[9] D. Albers *et al.* (EDDA Collaboration), Eur. Phys. J. A **22**, 125 (2004).

[10] M. Altmeier *et al.* (EDDA Collaboration), Eur. Phys. J. A **23**, 351 (2005);

[11] F. Bauer *et al.* (EDDA Collaboration), Phys. Rev. C **71**, 054002 (2005).

[12] P. Adlarson *et al.*, Phys. Rev. Lett. **112**, 202301 (2014); Phys. Rev. C **90**, 035204 (2014).

[13] R. L. Workman, W. J. Briscoe, and I. I. Strakovsky, Phys. Rev. C **93**, 045201 (2016); R.L. Workman, EPJ Web Conf. **81**, 02023 (2014).

[14] J. Ball *et al.*, Nucl. Phys. A **559**, 477 (1993); **559**, 489 (1993).

[15] R. A. Arndt, C. H. Oh, I. I. Strakovsky, R. L. Workman, and F. Dohrman, Phys. Rev. C **56**, 3005 (1997).

[16] R. A. Arndt, I. I. Strakovsky, and R. L. Workman, Phys. Rev. C **62**, 034005 (2000).

[17] R. A. Arndt, I. I. Strakovsky, and R. L. Workman, *ibid.* **50**, 2731 (1994).

[18] R. A. Arndt, L. D. Roper, R. L. Workman, and M. W. McNaughton, Phys. Rev. D **45**, 3995 (1992).

[19] M. Bashkanov *et al.*, Phys. Rev. Lett. **102**, 052301 (2009); P. Adlarson *et al. ibid.* **106**, 242302 (2014); Phys. Lett. B **721**, 229 (2013); Phys. Rev. C **88**, 055208 (2013); Phys. Lett. B **743**, 325 (2015)

[20] D. Mchedlishvili *et al.*, Phys. Lett. B **755**, 92 (2016).

[21] Z. Bagdasarian *et al.*, Phys. Lett. B **739**, 152 (2014).

[22] The SAID [http://gwdac.phys.gwu.edu] website provides access to both fits, models and the associated databases.

[23] R. A. Arndt, J. S. Hyslop, and L. D. Roper, Phys. Rev. D **35**, 128 (1987).

[24] D. Bugg *et al.*, Phys. Rev. 146 980 (1966).

[25] B. J. ver West and R. A. Arndt, Phys. Rev. C **25**, 1979 (1982).

[26] J. Bystricky, F. Lehar, and P. Winternitz, J. Phys. (Paris) **39**, 1 (1978).

[27] V. G. J. Stoks, R. A. M. Klomp, M. C. M. Rentmeester, and J. J. de Swart, Phys. Rev. C **48**, 792 (1993); V. G. J. Stoks, R. A. M. Klomp, C. P. F. Terheggen, and J. J. de Swart, Phys. Rev. C **49**, 2950 (1994); V. G. J. Stoks, private communication, 1995.